Title

3D fatigue crack path deflection and residual stresses in 17-4PH stainless steel rod

Authors

Shoemaker, Trevor K

Harris, Zachary D

Smudde, Christine M

et al.

Publication Date

2023-10-01

DOI

10.1016/j.ijfatigue.2023.107735

Revised: 5/16/2023

3D Fatigue Crack Path Deflection and Residual Stresses in 17-4PH Stainless Steel Rod

Trevor K. Shoemaker*, Zachary D. Harris*, Christine M. Smudde**, Michael R. Hill***, James T. Burns‡,*

‡Corresponding author. E-mail: jtb5r@virginia.edu.
*Department of Materials Science and Engineering, Center for Electrochemical Science and Engineering, University of Virginia, 395 McCormick Road, P.O. Box 400745, Charlottesville, Virginia 22904-4745.
**Department of Materials Science and Engineering, University of California, Davis, 1 Shields Ave, Davis, CA 95616.
***Department of Mechanical and Aerospace Engineering, University of California, Davis, 1 Shields Ave, Davis, CA 95616.

Authors' final version of manuscript accepted for publication in
International Journal of Fatigue 175 (2023) 107735
Available on-line at https://doi.org/10.1016/j.ijfatigue.2023.107735

Abstract

Damage tolerant structures require accurate fatigue crack growth rate models for life prediction. Central to these models are fracture mechanics similitude and empirically gathered growth rates. In this work, standard test methods failed to achieve similitude for 17-4PH stainless steel round-rod but succeeded for plate. Material product form differences are interrogated through constant ΔK tests, crack path analysis, residual stress (RS) characterization, and growth rate simulation. Analyses revealed that quench-induced RS in the round-rod promoted a non-planar, 3D crack path with closure effects. Strategies to mitigate the RS/path effects are evaluated by controlling constraint, closure, environment, and heat treatment.

Keywords

17-4PH, Residual Stress, Crack Path, Closure, Material Product Form

Highlights

- Product form effects on fatigue crack growth are better described via grain structure, residual stress, and/or crack path differences.
- Quenching-induced residual stress states may promote 3D fatigue crack paths.
- Growth rate prediction via residual stress superposition is hampered by 3D crack path-induced closure.
- Non-planar crack paths induced by residual stress are resilient to mitigation without heat treatment.

Text

1.0 Introduction

Fatigue is a prominent failure mode for metallic structures used in engineering applications[1]. Specifically, cyclic loading of a sufficient magnitude will induce a fatigue damage accumulation process resulting in crack nucleation, growth, and eventual fracture. This has motivated the development of several paradigms[2–4] for predicting and/or managing the subcritical cracking associated with fatigue. Of these, the damage-tolerance paradigm[5] is widely utilized in the aerospace industry where safety-of-flight structures are commonly subject to fatigue-critical conditions. This damage-tolerance paradigm relies on an assumed initial flaw that grows based on known material-loading interactions resulting in a predictable component life (i.e., number of load cycles to failure). Fundamentally, this approach to structural life management depends on translating empirically-measured fatigue crack growth rates from an exemplar material coupon[6] to a more complex structure composed of the same material type. This translation is enabled by and depends on the idea of fracture mechanics similitude[7].

The reliance of the damage tolerance paradigm on empirically-measured fatigue crack growth rates underscores the importance of factors that can affect a measured growth rate. For engineering purposes, the fatigue crack growth rates are typically presented as a function of a stress intensity range (ΔK) and stress ratio (R)[8]. Based on the fracture mechanics similitude principle alone, these two factors should be sufficient to specify the fatigue crack growth behavior of a material, so processes and guidelines for reliably obtaining these datasets are provided in standards like ASTM E647[6]. However, standard test conditions may fail to capture many nuances that can drastically affect a fatigue crack growth rate. As a few examples, the fatigue crack growth rate is subject to modification through differences in short versus long crack behavior[9], microstructural influences on the damage process[10], growth retardation due to variations in load waveform[11], residual stress effects[12,13], crack path-based modifications to the stress intensity[14], environmental impacts on crack growth[15], and crack closure[16]. These various modifiers can act alone or together to produce order of magnitude changes in a measured fatigue crack growth rate for a given ΔK-R-material combination. Critically, these crack growth rate modifiers can strongly impact downstream component life prediction and safe management of structures.

One modifier that may affect fatigue crack growth behavior is the material product form (e.g., plate, sheet, extrusion, etc.). The effect of form on fatigue crack growth behavior has been previously evaluated for several material systems with varying conclusions. Studies evaluating form effects in IN 718[17] and A-286 steel[18] noted no significant differences in fatigue crack growth behavior. Conversely, a comparison of hot rolled and cold drawn NiTi noted a significant reduction in fatigue threshold stress intensity range in

the cold drawn material[19]. Numerous studies have been devoted to form effect in Al alloys. Kaufman notes that recrystallization occurring in Al extrusions can have significant effects on fatigue behavior[20]. This recrystallization effect is further supported by Venkateswara et al. who found different fatigue behaviors for Al-Li plate and recrystallized sheet[21]. Saxena and Radhakrishnan further noted that Al-Li plate thickness can affect the fatigue crack growth behavior via differences in crack path roughness induced closure behavior[22]. However, grain structure effects in Al forgings were evaluated via comparison to Al plate by Bush et al., and differences in fatigue crack growth behavior were attributed to residual stress effects rather than the grain structure[23]. Taken together, these studies indicate that the material form effect on fatigue might be better described via sub-factors such as grain structure, residual stress, or resultant crack path differences. The latter two factors are of interest in the current work.

The residual stress in a material may be both (1) a function of the processes involved in producing a material product form and (2) a key factor affecting fatigue crack growth behavior. Product form residual stresses are typically caused by inhomogeneous plastic deformation induced during cooling of a material after processes like hot-rolling[24] or during quench cooling required for heat treatment[25]. The shapes and magnitudes of such residual stress distributions are complex functions of the cooling rate[26], product form shape[27], and the elevated temperature mechanical behavior of the material. These residual stresses may then modify an applied stress ratio via superposition to produce a total stress ratio (R_{tot}) and subsequently affect the fatigue crack growth rate[28]. This superposition paradigm has successfully accounted for the effect of residual stress on fatigue crack growth in many situations[12,29,30]. However, in some cases residual stress may cause additional closure[31,32] and/or crack path[33,34] behaviors that further complicate fatigue crack growth rate prediction. Of these, residual stress effects on crack path are particularly concerning since damage tolerance analyses typically assume a flat fatigue crack path with a semi-circular or straight crack front[35]. In a similar manner to residual stress, the shape of a crack can modify the fatigue crack growth rate. Engineering approaches exist to account for kinked cracks[36] (i.e., planar 2-D deflection from the Mode I path) and complex crack fronts[37] (i.e., planar but non-straight/non-elliptical through thickness), but fully 3-D crack paths that include twist[38–41] (i.e., non-planar) are rarely considered or characterized.

The interrelationship of material product form, heat treatment, residual stress, crack path, and closure impacts on the fatigue crack growth rate motivates the current work. In laboratory scenarios, such modifiers to the fatigue process can be individually controlled and/or eliminated via various techniques in order to obtain the "intrinsic" fatigue crack growth rate of a material. For example, residual stress may be minimized through a stress-relief heat treatment[42] or a planar crack path may be promoted through side-grooving[43], but this elimination/control strategy can become difficult without *a priori* knowledge of the particular, active modifiers. The current study highlights a case where standard, fracture mechanics-based

fatigue crack growth rate measurement techniques produced anomalous growth rate and 3D crack path behaviors that compromised fracture mechanics similitude. Specifically, similitude was compromised during testing of a round rod form of 17-4PH stainless steel but was not compromised for an equivalent-strength plate form of the same alloy. Differences in fatigue behavior for steel product forms with similar strength and microstructures are typically considered to be minimal, so the objective of this work is to quantify these anomalous fatigue behaviors and systematically investigate their microstructural and mechanistic origins. The effectiveness of fatigue process modifier elimination/control strategies like constraint modification, closure control, environment control, and heat treatment are applied and evaluated via constant ΔK test strategies. The study concludes with characterization of residual stress in the 17-4PH rod and an assessment of the role of residual stress in these fatigue crack growth behaviors.

2.0 Methods

2.1 Materials

Two material product forms of 17-4PH stainless steel were obtained from commercial suppliers and evaluated during this study. The first form was electric furnace (EF) melted, argon oxygen decarburized (AOD), hot-rolled, and centerless ground 15.9 mm diameter round rod (hereafter referred to as "rod"). The second form was EF melted, AOD refined, and hot-rolled 15.9 mm thick plate (hereafter referred to as "plate"). Both forms were solution annealed by their respective manufacturers, constituting the "As Received" (AR) condition. The manufacturer for the rod indicated a 1040°C/1 h/air cool solution anneal while the plate manufacturer indicated a 1040°C solution anneal for an unspecified time with an unspecified cooling rate. Elemental compositions for both forms of 17-4PH were measured by a commercial lab via glow discharge mass spectroscopy and inductively coupled plasma optical emission spectroscopy, refer to Table 1. A variety of heat treatments were performed on the materials after receipt, refer to Table 2. The H900 and H1025 heat treatment conditions represent common engineering tempers for peak strength or increased toughness[44], respectively. The SA condition represents the effects of a second solution anneal. Tensile testing was performed in accordance with ASTM E8[45] at a constant displacement rate of $8\text{x}10^{-4}$ mm/s with an 8 mm gage length clip-on extensometer to measure modulus of elasticity (E), yield strength (σ_{YS}), ultimate strength (σ_u), and engineering strain at failure (e_f). Rockwell hardness (HRC) was determined via Vickers hardness measurements that were converted to HRC in accordance with ASTM E384/E140[46,47].

Microstructure was evaluated using the electron backscatter diffraction (EBSD) technique and electrolytic etching. Samples were prepared by mounting in cold-curing epoxy resin, incrementally grinding using 320/600/800/1200 grit paper, polishing incrementally using 3/1/0.5/0.25/0.1 μm polycrystalline diamond slurries, and finish polishing using 0.05 μm alumina or colloidal silica. Multiple material planes

Table 1 | **Elemental compositions of the 17-4PH plate and rod used in this study in weight %.**

Form	C	Mn	P	S	Si	Cr	Ni	Cu	Nb	Fe
Plate	0.041	0.51	0.018	0.001	0.32	15.20	4.85	3.22	0.26	bal.
Rod	0.034	0.41	0.017	0.001	0.66	14.80	4.70	3.11	0.26	bal.

Table 2 | **Heat treatment codes/designations and associated processing parameters used in this study.**

Heat Treat Code	Processing Details
AR - As Received	Solution annealed by the manufacturer.
H900 - Peak Aged	AR; Machined specimen; 482°C/1 h in lab air, air cool.
H1025 - Overaged	AR; Machined specimen; 552°C/4 h in lab air, air cool.
SA - Solution Annealed	AR; 1040°C/0.5 h in lab air, air cool; Machined specimen.

(i.e., relative to the hot-rolling direction) were examined for each form of material where L, T, S, R, C refer to the in-plane long (rolling), long-transverse, short-transverse, radial, and circumferential directions, respectively. Orientation imaging microscopy (OIM) via EBSD was performed using a FEI Helios G4 UC FIB/SEM equipped with an Oxford Instruments Symmetry EBSD detector. Inverse pole figure (IPF) maps were constructed from the OIM data using the MTeX software package[48], and prior austenite grain boundaries were reconstructed using methods provided by Nyyssönen et al[49]. Select samples were electrolytically etched in 5 M NaOH at 23°C with a direct current power supply (20 V for 20 s) and stainless-steel wire counter electrode to reveal delta ferrite distributions via optical microscopy.

2.2 Fatigue Crack Growth Rate Measurement

Fracture mechanics-based fatigue crack growth rate testing was performed using a servo-hydraulic load frame applying sinusoidal waveforms. Crack length (a) was continuously monitored using the direct current potential difference (DCPD) method[50]. A closed-loop feedback system monitoring the crack lengths and loads enabled stress intensity (K) controlled loading. The single edge notch tension (SENT) specimen geometry was utilized with a 2.67 mm thickness (B) and 12.20 mm width (W) gage section ($B/W = 4.6$). A single test specimen was side-grooved using 0.05 mm groove radii and a reduced thickness of 2.10 mm (B_N), all other SENTs were flat-sided. Each SENT had an electrical discharge machined (EDM) pre-notch with a 0.940 mm length and 0.038 mm root radius. The plate and rod SENTs were oriented in the L-T and L-R Mode I loading-crack growth directions[51], respectively, and removed at the center of the stock thickness (plate) or diameter (rod). Primary fixturing consisted of a pinned-pinned loading configuration with linear elastic K calculations[52] for the flat-sided SENTs. For the side-grooved SENT, the same K-solution was utilized, but with $B = \sqrt{B \cdot B_N}$ as recommended by Freed et. al[53]. A single test was performed in a "fixed-fixed" configuration by orienting the SENT orthogonal to the rotational plane of the pin (i.e., to preclude crack mouth "yawning" allowed by the pins). This fixed-fixed test used a K-solution provided by Zhu[54] for clamped SENT specimens ($H/W = 3.14$, where H is the distance between the clamp constraints).

Environmental control was obtained by affixing an acrylic cell around the SENT gage section and flowing N_2 gas either dry (RH ~ 0%) or humidified by bubbling through deionized water (RH > 90%). Otherwise, testing was performed in lab air with RH ~ 50%.

Fatigue test protocols consisted of either a stress intensity range (ΔK) shed/rise or a constant ΔK test. In both cases, testing was preceded by pre-cracking 0.250 mm out of the pre-notch at a constant ΔK = 6.3 MPa√m and R = 0.1. For the shed/rise tests, a shed was first performed to find the threshold stress intensity range (ΔK_{th}) at $da/dN \sim 10^{-7}$ mm/cycle per ASTM E647[6]; the shed was performed at a normalized K-gradient (C) of either -0.08 mm^{-1} as recommended by ASTM E647 or a more aggressive C = -0.75 mm^{-1}. After the shed, the rising ΔK portions of the tests were performed with either C = 0.5 mm^{-1} or a constant amplitude load until a specified maximum ΔK or fast-fracture. Constant ΔK tests were performed at ΔK = 9 MPa√m starting at the end of the precrack and typically ending at a normalized crack length (a/W) of 0.8. All testing was performed at a loading frequency of 10 Hz and fixed stress ratio (R). Post-test, fracture surfaces were examined using a combination of optical microscopy and white light interferometry. Each fracture surface was measured using optical microscopy to verify dcPD-calculated crack lengths[55]. The in-situ and post-test measured crack lengths were within typically 0.1 mm of each other. Fracture surface topography was captured using white light interferometry with a Zygo NewView 7300. Topographic data was gathered using a 2.5x objective with a 10.3 mm working distance and a low-resolution Frequency Domain Analysis (FDA). Extended scans were used to traverse the high peaks and low valleys while automatic stitching routines were used to cover the length and width of the fracture surface. Post processing was performed using MountainsMap® version 7.4 to remove data outliers, level the topography data based on the plane of the pre-notch, calculate/plot surface roughness (Rq)[56], and plot/extract topographic data.

2.3 Residual Stress Measurement

Axial residual stresses (σ_{RS}) that cause residual stress intensity factors (K_{RS}) were measured on a plane parallel to the Mode I crack plane in selected samples using the incremental slitting method[57]. The slitting method determines an average through-thickness residual stress acting normal to a specified plane as a function of position across the plane (i.e., a line profile of residual stress acting to open or close the slit). In general, the slitting method involves incrementally cutting from the front face of the sample toward the back face on the plane of measurement. With each cut, a strain gage attached on the sample back face is used to measure change in strain as a function of incremental cut depth. This strain versus cut depth data enables calculation of residual stress versus position from the front face[57,58] as well as the residual stress intensity factor[59].

The slitting method in this work followed established experimental and data reduction practices[57] used to account for residual stress effects on fatigue crack growth rate behavior[12,28]. In this particular case,

slitting measurements were performed on square shaped samples of dimensions W x W x B cut adjacent to the crack path of selected SENT samples after fatigue crack growth rate testing as illustrated in Fig. 1. A slitting plane parallel to the nominal crack path for each sample was cut by wire EDM in 41 equal increments to a total depth of $0.95W$. The incremental strain versus depth measurements were then used to calculate σ_{RS} and K_{RS} as a function of a/W. Residual stress calculation followed the approach described by Schajer and Prime[60] which includes regularization to reduce sensitivity to noise in the strain data. $K_{RS}(a)$ was calculated using Schindler's method for a thin rectangular plate[61]:

$$K_{RS}(a) = \frac{E'}{Z(a)}\frac{d\epsilon}{da} \quad \textbf{(1)}$$

The calculation uses the plane stress modulus of elasticity (E' = E), the influence function for a square plate ($Z(a)$), and the derivative of strain with respect to slit depth ($d\epsilon/da$). The strain derivative was computed using a 5-point moving parabolic fit to strain versus slit depth data. Note that the prior fatigue testing loads were within the elastic regime, and the slit was far away from the crack tip stress zone. Therefore, loading-induced residual stress relaxation was likely small. However, the measured residual

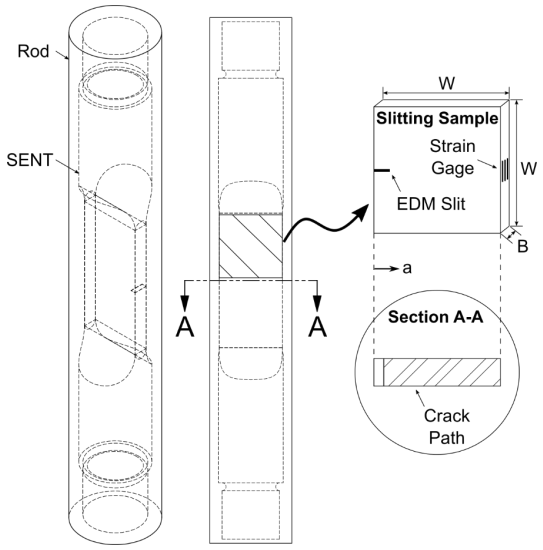

Fig. 1 | **Schematic of samples used for residual stress measurement via the slitting method**. SENT samples were machined from 17-4PH rod and fatigue tested along the nominal crack path identified in Section A-A. After fatigue testing, a portion of the SENT adjacent to the crack path was excised for use as a slitting sample, instrumented with a strain gage, and incrementally slit via EDM. Strains measured during the slitting process were used to calculate residual stress as a function of crack length (a) normalized by the SENT width (W) (i.e., a/W).

stresses and stress intensity factors were likely somewhat smaller than those that acted during the fatigue tests due to the smaller size of the slitting samples compared to the SENT samples[62]. Error bars on σ_{RS} in this work quantify the slitting model error/uncertainty[63], but do not account for the sample size effect.

2.4 Fatigue Crack Growth Rate Simulation

The NASGRO equation[64,65] simulated the effect of residual stress on fatigue crack growth rate via superposition of a measured residual stress intensity (K_{RS}) on a nominal, applied stress intensity waveform (K_{app}). These methods are described in the NASGRO software manual[65] and are briefly reviewed below. First, the nominal stress ratio ($R = K_{app,min}/K_{app,max}$) was transformed into a total stress ratio (R_{tot}) by superimposing the applied and residual stress intensity factors:

$$R_{tot} = \frac{K_{app,min} - K_{RS}}{K_{app,max} - K_{RS}} \tag{2}$$

Plasticity induced closure effects were then estimated using the Newman model[66]. This yields a closure function (f) of the form below that depends on the effective stress ratio where K_{op} and K_{max} are the opening and maximum stress intensities for a load waveform, respectively.

$$f[R_{tot}] = \frac{K_{op}}{K_{max}} \tag{3}$$

The closure corrected threshold stress intensity range (ΔK_{th}) was then calculated as follows. Note that m, p, ΔK_1, C_{th}, and A_0 are empirical material parameters for the NASGRO equation.

$$\Delta K_{th} = \frac{\Delta K_1 \left(\frac{1 - R_{tot}}{1 - f[R_{tot}]}\right)^{1+R_{tot}C_{th}^p}}{(1 - A_0)^{(1-R_{tot})C_{th}^p}}, R_{tot} \geq 0$$
$$\Delta K_{th} = \frac{\Delta K_1 \left(\frac{1 - R_{tot}}{1 - f[R_{tot}]}\right)^{1+R_{tot}C_{th}^m}}{(1 - A_0)^{C_{th}^p - R_{tot}C_{th}^m}}, R_{tot} < 0 \tag{4}$$

Then, the thickness corrected fracture toughness (K_c) was estimated as follows where K_{1c} is the plane strain fracture toughness, t is the specimen thickness ($t = B$), and A_k, B_k are additional material parameters.

$$K_c = K_{1c}\left(1 + B_k e^{-\left(A_k \frac{t}{t0}\right)^2}\right) \tag{5}$$

$$t_0 = 2.5\left(\frac{K_{1c}}{\sigma_{YS}}\right)^2 \tag{6}$$

Finally, a simulated fatigue crack growth rate was calculated using the NASGRO equation[64] where C_N, n, and q are additional material parameters:

$$\frac{da}{dN} = C_N \left[\frac{1 - f[R_{tot}]}{1 - R_{tot}} \Delta K\right]^n \frac{\left(1 - \frac{\Delta K_{th}}{\Delta K}\right)^p}{\left(1 - \frac{K_{max}}{K_c}\right)^q} \quad \textbf{(7)}$$

Note that values for the empirical material parameters in this approach (e.g., p, m, C_{th}, etc.) were based on the built-in parameters provided by the NASGRO 9.1 software package for 17-4PH (H900, plate, L-T, material code: G2CB11AB1) and are, therefore, unlisted.

3.0 Results & Discussion

3.1 Microstructure & Mechanical Properties

Microstructural analysis and mechanical evaluation showed minor differences between the rod and plate material forms of 17-4PH in this study. As shown in Fig. 2, both materials had martensitic grain structures with similar martensite block sizes (Fig. 2a,d). Reconstruction of the prior austenite grain (PAG)

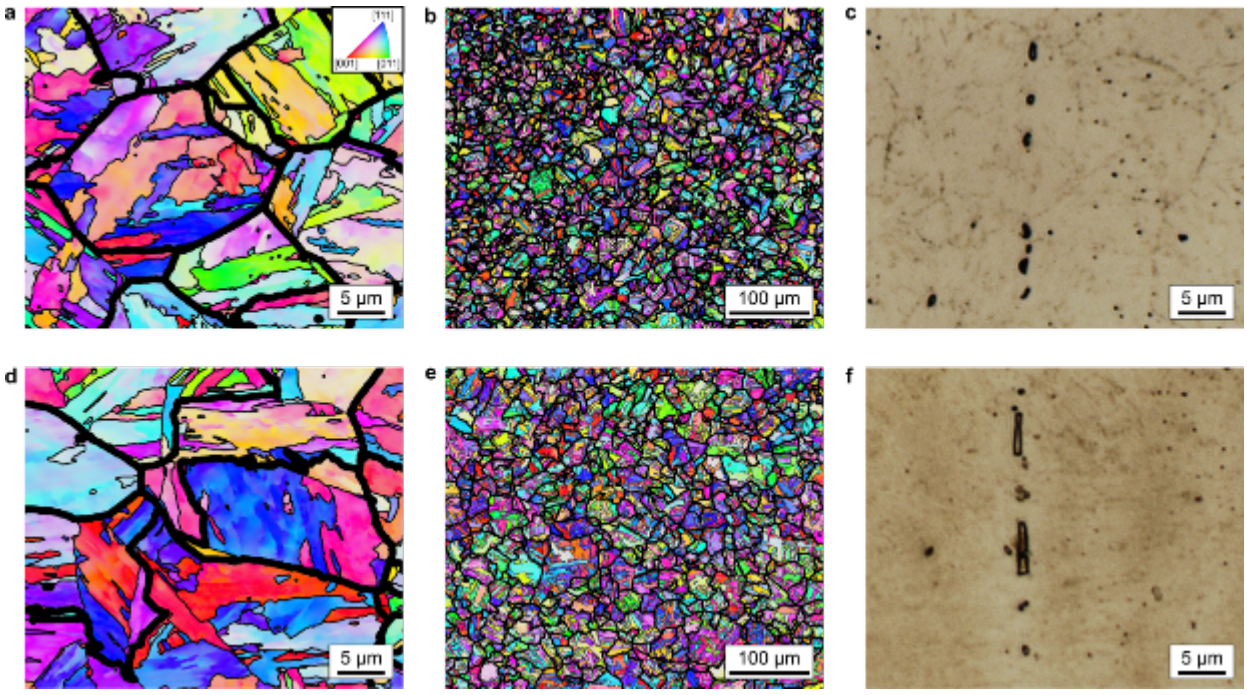

Fig. 2 | **Comparison of 17-4PH rod and plate microstructures**. **a-c**, 17-4PH plate microstructure. **d-f**, 17-4PH rod microstructure. Representative microstructure images are shown for 17-4PH plate (**a**, **b**, **c**) and rod (**d**, **e**, **f**). Grain orientation imaging maps are shown in (**a**, **b**, **d**, **e**) with bold and fine black outlines highlighting the PAG and martensite block boundaries, respectively. The most severe cases of delta ferrite stringers observed in each material form are shown in (**c**, **f**) with the L direction aligned vertically.

boundaries showed equiaxed grains in both cases with a slightly coarser grain structure in the rod (Fig. 2b,e). Small quantities of delta ferrite aligned with the rolling direction, typical of 17-4PH[67], were present in both materials with the most severe cases shown in Fig. 2c,f. Phase analysis showed a negligible amount of retained austenite appearing as small (~3 μm), widely spaced islands in both materials (images not shown). Broader area analyses confirmed these basic observations across multiple material planes (i.e., LT, LR, ST, etc.). Compositionally, both materials met their respective ASTM A564/A693[44,68] requirements, though the rod had double the Si content of the plate (Table 1). Similarly, mechanical evaluation of selected tempers of the materials showed that both met ASTM A564/A693[44,68] requirements with the rod generally having higher strength/hardness and lower ductility than the plate (Table 3).

3.2 Comparing 17-4PH Rod and Plate Fatigue Responses

Fatigue crack growth rates (*da/dN*) in humidified air as a function of stress intensity range (ΔK) were compared for 17-4PH rod and plate in the H900 condition at R = 0.5 and R = 0.7 (Fig. 3). At R = 0.5, growth rates were obtained at a variety of normalized K-gradients (C). In particular, the ASTM E647 recommended C = -0.08 mm^{-1} was used during the ΔK shed for the rod while the plate was tested at a much more aggressive C = -0.75 mm^{-1}. In the case of the plate, there was good correspondence in *da/dN* between the shed and the subsequent ΔK rise. Conversely, there was an anomalous, order of magnitude mismatch in growth rate between the ΔK shed and rise for the rod with a maximum growth rate mismatch occurring at ΔK = 9 MPa√m. This mismatch yielded an apparent threshold stress intensity range (ΔK_{th}) of 7 MPa√m for the rod while ΔK_{th} = 3 MPa√m for the plate. In the Stage II growth region, the plate displayed a typical, Paris-law behavior while the rod had a nonlinear transition to Stage III growth behavior. In Stage III, the plate cracked without fracture until the test was halted at ΔK = 50 MPa√m while the rod fast fractured at ΔK = 40 MPa√m. A more direct comparison of crack growth rates between the plate and rod was performed at R = 0.7 with matched C = 0.5 mm^{-1} (Fig. 3b). The aforementioned observations at R = 0.5 are largely similar at R = 0.7. Notably, the shed/rise growth rate mismatch for the rod recurred at R = 0.7 – though with a reduced magnitude.

Table 3 | **Mechanical properties for selected tempers of the 17-4PH plate and rod used in this study.**

Form	Heat Treat	HRC	σ_{YS} (MPa)	σ_u (MPa)	E (GPa)	e_f (%)
Plate	H900	44	1194	1336	204	41
	H1025	37	1059	1110	207	44
Rod	H900	46	1410	1412	202	37
	H1025	38	1094	1099	199	42

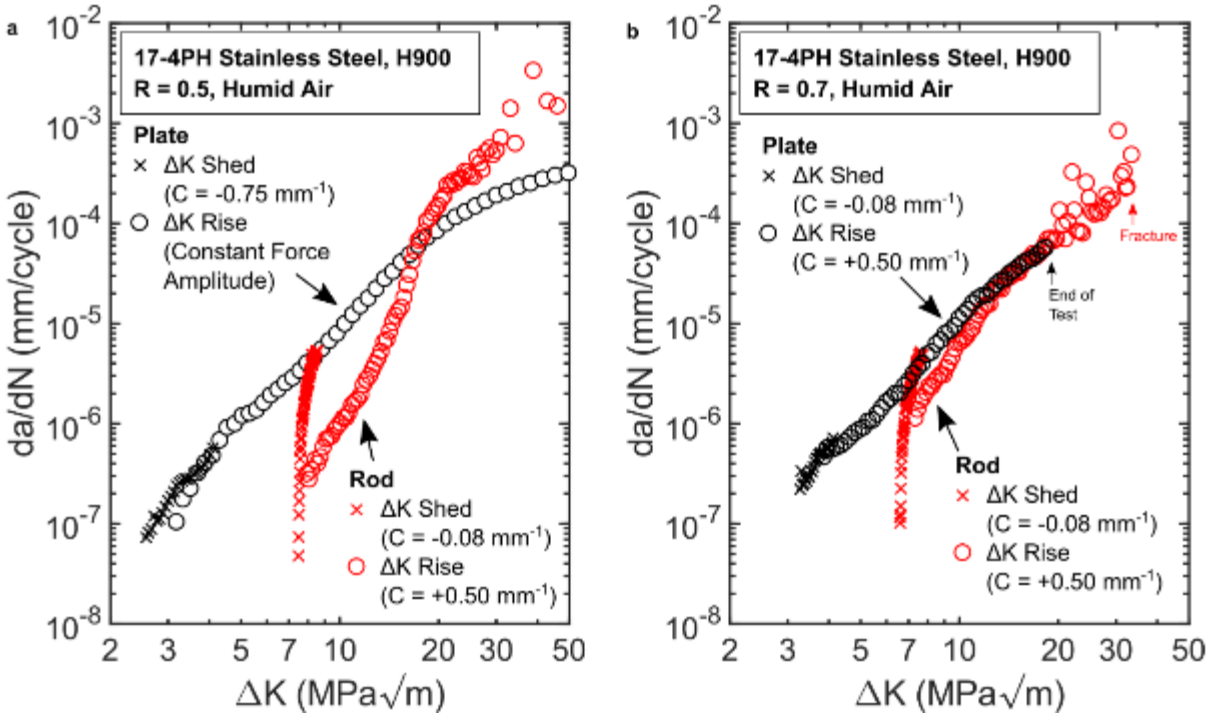

Fig. 3 | **Comparison of fatigue crack growth rates for 17-4PH rod and plate in humid air**. **a**, R = 0.5. **b**, R = 0.7. Fatigue crack growth rate (da/dN) versus stress intensity range (ΔK) in humid air (>90% RH) for 17-4PH plate and rod are compared at R = 0.5 (**a**) and R = 0.7 (**b**). Growth rates gathered under shedding or rising ΔK are identified along with the normalized K-gradients (C) used to control load application.

Given the significant differences in ΔK_{th} between the rod and plate and the apparent breakdown of linear elastic fracture mechanics (LEFM) similitude between the ΔK shed and rise for the rod, understanding the "mismatch" behavior in the rod was of interest. To begin investigating this mismatch phenomenon, constant ΔK = 9 MPa√m fatigue crack growth rates as a function of normalized crack length (a/W) were gathered for the two material forms (Fig. 4a). If fracture mechanics similitude holds then a constant ΔK test should produce a constant crack growth rate for all a/W at a given ΔK and R. For the plate, the crack growth rate was nominally constant at $6\text{x}10^{-6}$ mm/cycle across all tested a/W – consistent with Fig. 3a. The rod, however, exhibited a crack growth rate that varied from $5\text{x}10^{-7}$ mm/cycle up to $8\text{x}10^{-6}$ mm/cycle with two local growth rate minima occurring at a/W = 0.39 and 0.77. Note that a/W = 0.5 for the rod corresponded to the centerline of the parent rod stock material while all a/W for the plate were confined to the center plane of the parent plate stock material. Topographic maps of the fracture surface from white light interferometry showed that the plate fracture path is relatively flat with Z height variation less than 100 µm (Fig. 4b). Conversely, the fracture surface of the rod was twisted at intermediate a/W with the maximum peak to valley exceeding 200 µm and approximately aligning with the anomalous growth rate trough.

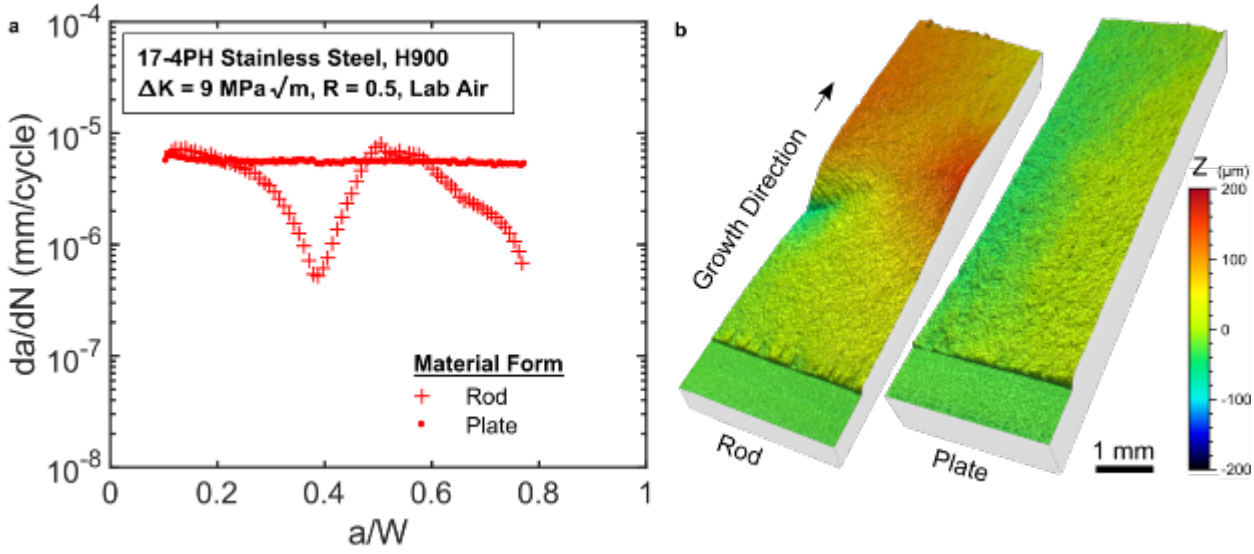

Fig. 4 | **Comparison of 17-4PH rod and plate fatigue behavior at constant *ΔK*.** **a**, Fatigue crack growth rate versus normalized crack length (*a/W*). **b**, Fatigue fracture topographies. Growth rates were captured in lab air as a function of *a/W* at a constant ΔK = 9 MPa√m, R = 0.5 for 17-4PH rod and plate in the H900 condition (**a**). Topographic height (Z) maps of the fracture surfaces from (**a**) are shown in (**b**). The primary growth region in (**b**) is preceded by EDM notch (0.94 mm) and precrack (0.25 mm) regions. Note also that the 1 mm scalebar in (**b**) only applies to planar dimensions; Z height is exaggerated for clarity.

These data show substantial fatigue crack growth behavior differences between the rod and plate product forms of 17-4PH in the H900 condition. The plate fatigue crack growth behavior was well-characterized using standard ASTM E647 guidelines. Fracture mechanics similitude and classical Paris-law behavior in the plate suggests that its intrinsic fatigue behavior was captured. However, the rod has anomalous (1) order of magnitude differences in growth rate between the ΔK shed and rise, (2) variable fatigue crack growth rates at a constant ΔK, and (3) crack path twisting that corresponds to the variable growth rates. The breakdown of LEFM similitude and deviation from the Mode I crack path in the rod suggests that the fatigue fracture process was affected by one or more modifiers. These observations lead to the following questions:

1. What were the microstructural and/or mechanistic origins of the modifiers producing the anomalous 17-4PH rod fatigue behaviors?
2. Are there strategies that can effectively attenuate/eliminate these modifiers in order to obtain the intrinsic fatigue crack growth behavior of the 17-4PH rod?

There are a number of known fatigue mechanisms that could result in the growth rate and/or non-flat crack path. With regard to the crack path, fatigue crack path deflection can be induced by material influences, mechanical influences, and/or environmental influences. Specifically, material crystallographic

grain texture[69] and fracture along secondary phase(s) (e.g., along delta ferrite[70]) have both been demonstrated to influence a crack path. Mechanically, a form of out of plane cracking called "shear lipping"[71] has been linked to reduced crack tip constraint near free surfaces[43], *T*-stresses have been linked to out of plane cracking[72], and secondary stress fields (e.g., residual stress) can drive cracks out of plane[33]. Environmental interactions with the fatigue process have also been demonstrated to influence the crack path[73,74]. With regard to the variable growth rate, it is notable that the rod growth rate is generally lower than the plate fatigue crack growth rate (Fig. 4a). The crack path itself could reduce the growth rate since deviation from a flat, Mode I crack path will result in a reduction of mechanical driving force at the crack tip[75]. Another common means for growth rate deceleration is crack closure, though closure is a broad phenomenon with several possible sub-mechanisms[76]. In order to determine the true origin(s) of the observed crack path and growth rate behaviors, a variety of additional testing and characterization strategies were employed to systematically interrogate each of these potential mechanisms.

3.3 Interrogating the 17-4PH Rod Fatigue Crack Growth Response

3.3.1 Effect of Closure

A mechanism that might explain the observed reduction in the 17-4PH rod crack growth rate is crack closure. Closure occurs when a cyclically loaded crack tip has an opening stress intensity (K_{op}) that exceeds the applied K_{min} which effectively reduces the stress intensity range at the crack tip (i.e., $\Delta K_{eff} = K_{max} - K_{op}$)[7,76]. Typically, closure is attributed to plasticity, fracture surface roughness, oxides, and/or residual stress[77] that might cause the two faces of a crack wake to impinge[16]. One way to reduce or eliminate the effect of closure is by increasing the stress ratio of the cyclic load waveform to promote a larger K_{min} so that $K_{min} > K_{op}$ and $\Delta K \geq \Delta K_{eff}$. This simple test for closure effects was performed on the 17-4PH rod as shown in Fig. 5. The magnitudes of the growth rate drops at *a/W* = 0.39 and beyond *a/W* = 0.50 clearly reduce with the increase in stress ratio, but remnants of the underlying phenomenon are still present. The results of this test indicate that closure might be playing some role in the growth rate reduction process, especially with the non-flat crack path that may lead to impingement at elevated *a/W* (Fig. 4b). However, the persistent form of the growth rate behavior and non-flat crack path at elevated *R* suggests that closure is not the root cause.

3.3.2 Effect of Constraint

Low crack tip constraint is a possible origin for the non-flat crack path in Fig. 4 which could, in turn, lead to the observed growth rate reductions. First, the linear elastic crack tip stress field may be described as an infinite series[78]. That stress field is typically characterized with the stress intensity factor

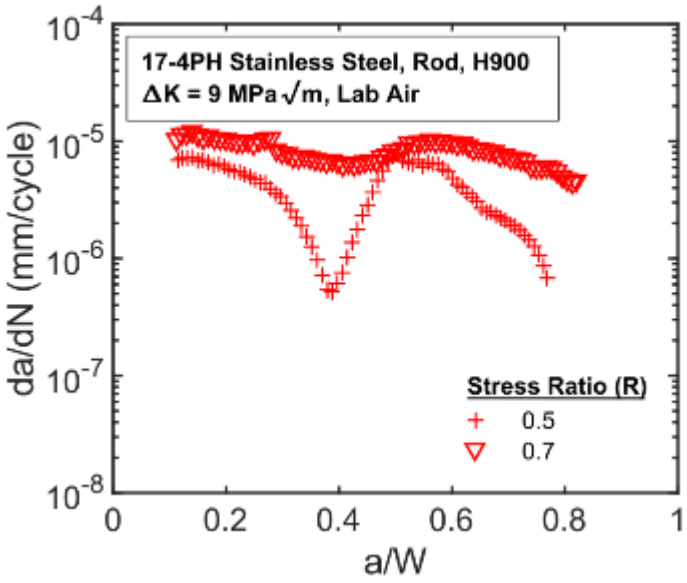

Fig. 5 | **Effect of stress ratio modification on fatigue crack growth in 17-4PH rod**. Fatigue crack growth rates are compared at two stress ratios (R = 0.5, 0.7) for 17-4PH rod in the H900 condition. Growth rates were captured in lab air as a function of a/W at a constant ΔK = 9 MPa√m.

(K) which is the dominant first term of the series, but the second term of the series contains a finite, "T-stress" acting parallel to the crack path[79]. Crack tip constraint may then be defined as the degree of crack tip stress triaxiality[7] and is sometimes estimated via the T-stress for linear elastic conditions[79]. An increase in crack tip constraint has been shown to promote a planar crack path[80]. One effect of low crack tip constraint is a non-planar crack path phenomenon called "shear lips"[71]. The current, twisted out of plane growth (Fig. 4b) bears some resemblance to shear lips that slant the fracture path near the free surface(s), so a shear lip-like behavior could be present. Second, a flat (i.e., minimally deflected) crack path results in a standard Mode I mechanical driving force for crack extension[81]. In the current case, the Mode I crack was deflected which would reduce the mechanical driving force and could have contributed to the observed growth rate reductions.

Several of the aforementioned hallmarks of low crack tip constraint are present in the 17-4PH rod in Fig. 4, so a side-grooved specimen was tested to evaluate the effect of increased constraint. One of the necessary conditions for shear lip formation is a state of plane stress that may be found at the free surface adjacent to a fatigue crack wake, so shear lips may be suppressed through the introduction of a notch adjacent to the wake to promote constraint and preclude plane stress conditions[71]. In fatigue testing, this behavior is utilized in "side-grooved"[53,82] specimens that increase crack tip constraint and reduce the likelihood for crack path deflection. The crack growth kinetics in Fig. 6 demonstrate that side-grooving had a negligible effect on the variable growth rate phenomenon in the rod. White light interferometry of

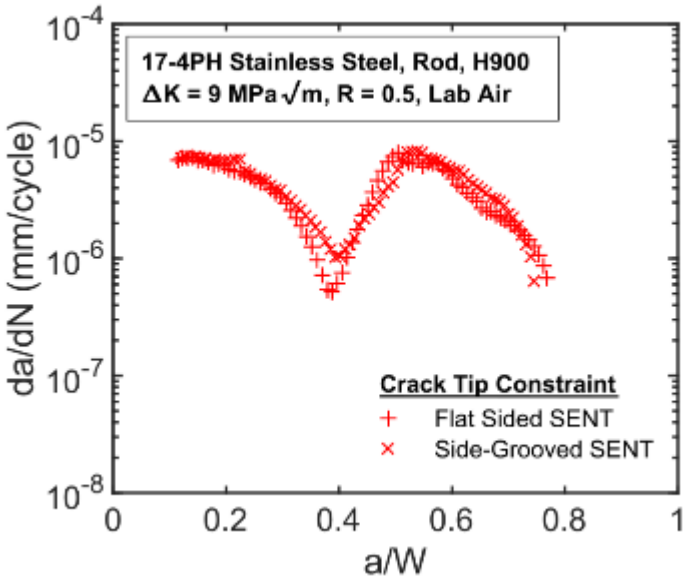

Fig. 6 | **Effect of crack tip constraint modification on fatigue crack growth in 17-4PH rod**. Different levels crack tip constraint were tested by fatigue cracking flat sided and side-grooved SENTs made from 17-4PH rod in the H900 condition. Growth rates were captured in lab air as a function of a/W at a constant ΔK = 9 MPa√m, R = 0.5.

the side-grooved sample also showed a non-flat crack path with local depressions at intermediate a/W in a similar manner to Fig. 4b. These results demonstrate that the current case of crack path deflection is not best described as a "shear lip" phenomenon, which should be sensitive to additional constraint. This is not particularly surprising as the condition of plane stress (i.e., low constraint) is only one of three conditions described as necessary for shear lip formation[71]. The two other conditions necessary for shear lip formation include (1) available material slip systems on the shear lip plane and (2) fast enough growth rate to permit shear lip initiation within one load cycle. Condition (1) was likely met, but condition (2) was likely violated given the low, decelerating growth rate occurring over hundreds of microns of crack extension and associated with the observed crack path deflection.

Regardless of the ineffectiveness of side-grooving to constrain the crack path, perhaps constraint was still the root cause of the crack path instability in the 17-4PH rod. As previously mentioned, the T-stress may be used to quantify the constraint of a crack tip stress field and is a function of the crack geometry, specimen geometry, and loading configuration[83]. One way to quantify the relative constraint of a growing crack is by plotting the biaxiality ratio (β) which is the ratio of the stress intensity (K) and the T-stress with a crack length factor to normalize units. Generally, a compressive β is associated with increased constraint and crack path stability whereas a tensile β will drive out of plane growth[80]. The differences in constraint for two loading configurations (pinned-pinned and fixed-fixed) of the SENT sample geometry are shown in Fig. 7a. The displayed β distributions both assume a normalized distance between the load

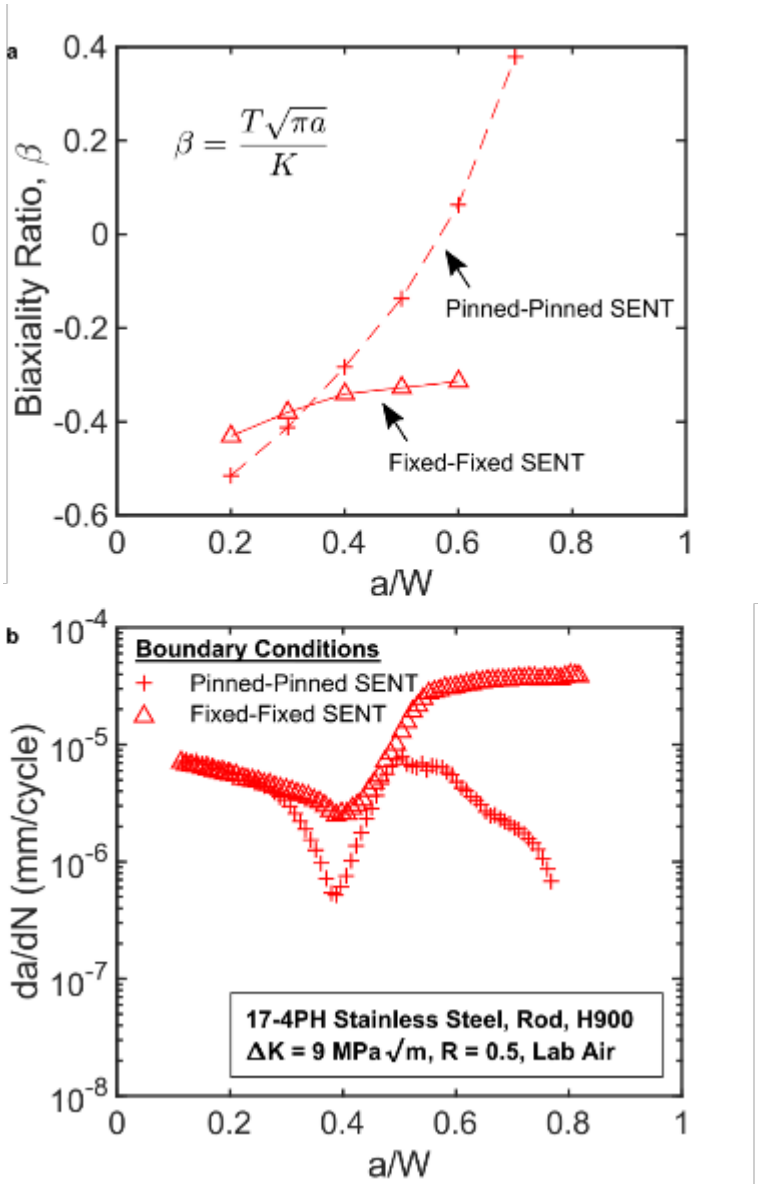

Fig. 7 | **Comparison of T-stress variation and its effects on fatigue crack growth in 17-4PH rod**. **a**, *T*-stress distributions via the biaxiality ratio (β) as a function of a/W in pinned-pinned and fixed-fixed SENT loading configurations. **b**, Fatigue crack growth rates versus *a/W* in pinned-pinned and fixed-fixed SENTs. Published *T*-stress distributions are compared for two SENT loading configurations (**a**). The effects of these *T*-stress distribution differences on fatigue crack growth rates were then tested on 17-4PH rod in the H900 condition at a constant ΔK = 9 MPa$\sqrt{m}$, R = 0.5 in lab air (**b**).

application points (*H/W*) of 5, but for pinned-pinned[80] and fixed-fixed[54,84] boundary conditions. Unlike side-grooving which primarily modifies the state of plane stress at the free surface adjacent to a crack front, the *T*-stress modifications in moving to a different loading configuration should affect the entire crack front. It is also notable that the pinned-pinned SENT configuration (used thus far) steadily transitions from a

compressive to a tensile β with the crossover point occurring at a/W~0.6. Conversely, a fixed-fixed SENT maintains a relatively steady, compressive β up to a/W of 0.6.

These differences in constraint between pinned-pinned and fixed-fixed SENT loading configurations motivated an additional test evaluating bulk constraint effects. Based on the previous discussions, the increased bulk constraint of the fixed-fixed SENT might attenuate the crack deflection and subsequent growth rate reductions in the 17-4PH rod. The fatigue test results in Fig. 7b show that the bounce in growth rate at a/W = 0.39 persisted with the change from a pinned-pinned to a fixed-fixed SENT configuration, though there is a generally upward trend in growth rate with increasing a/W. Note that the upward trend is likely due to imperfect scaling of the K solution used to control load application in the fixed-fixed configuration rather than T-stress impacts. It has previously been documented that subtle load train compliance differences can modify the fixed-fixed effective stress intensity, and the K-solution can require tuning for ideal results[85]. Regardless of this issue, the additional, bulk constraint involved with fixed-fixed load application did not sufficiently modify the crack tip stress state to produce a constant crack growth rate. Combined, the results in Fig. 6 and Fig. 7 suggest that the anomalous fatigue crack path and growth rate behavior in the rod were not a result of crack tip constraint effects.

3.3.3 Effect of Environment

Environmental interactions with the fracture process also have the potential to affect a crack path. Examples of this behavior include fracture along a secondary phase in stainless steel[73] or hydrogen embrittlement interactions inducing preferential interfacial fracture in an aluminum alloy[74]. Each of these cases had a much more extreme environment (i.e., high temperature water for the steel) or a much more susceptible alloy (i.e., aluminum) than the current case of stainless steel in humid air (Fig. 3). However, an inert environment (e.g., dry N_2 gas) test was performed to rigorously eliminate environmental influences as a potential cause for the fatigue crack growth anomalies. This test was performed on material in the H1025 temper condition, rather than the H900 temper evaluated thus far, to simultaneously investigate the effect of heat treatment.

The results in Fig. 8 give the first hints at the root cause of the anomalous crack growth behavior in the 17-4PH rod. First, the inert environment had little effect on the growth rate reduction at a/W = 0.39. There was an overall reduction in the inert environment growth rate compared to the test in lab air, but this is expected since humidity in the air is known to cause a general acceleration of fatigue crack growth[86]. More importantly, the growth rate depression in Fig. 8 was reduced in comparison to the previous tests in Fig. 6 and Fig. 7b. The primary difference between these tests was an increase in the tempering time and temperature for H1025. This indicates that microstructural evolution or thermal stress relief during heat treatment may have impacted the phenomena underlying the unique fatigue behavior in the rod.

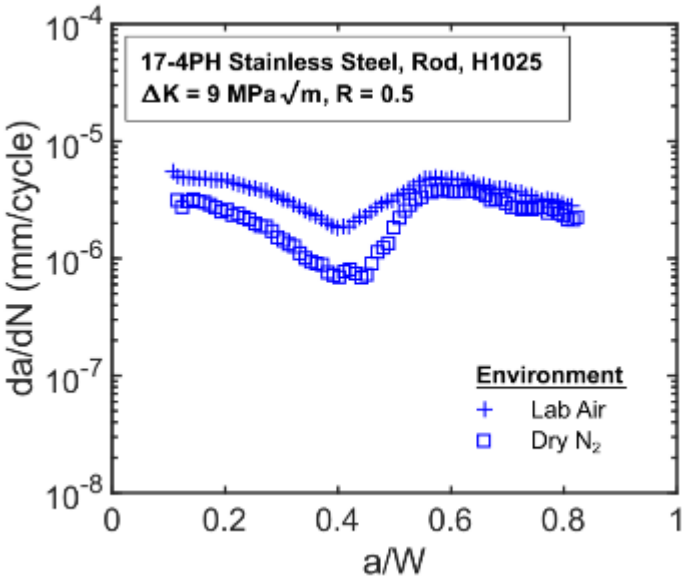

Fig. 8 | **Effect of environment modification on fatigue crack growth in 17-4PH rod.** Fatigue crack growth rates are compared in an inert (Dry N_2, RH ~ 0%) and benign (Lab Air, RH ~ 50%) environment for 17-4PH rod in the H1025 condition. Growth rates were captured as a function of a/W at a constant ΔK = 9 MPa√m, R = 0.5.

3.3.4 Effect of Heat Treatment

Given the clear impact of heat treatment on the variable crack growth rate in the 17-4PH rod, it is worth discussing the microstructural features in the alloy that might be affected by heat treatment. 17-4PH nominally consists of a martensitic matrix with small volume fractions of retained austenite, delta ferrite, micron-scale Nb carbides, and nano-scale Cu precipitates[87]. The Nb carbides are intended to sequester C during hot working[88] and are stable up to ~1300°C[89]. Additionally, hot working may result in delta ferrite stringers[90] that tend to be stable up to ~1040°C[67,91]. The martensitic matrix is stable up to ~700°C[89], and the commonly employed solution annealing treatments at 1040°C will produce an austenitic structure, dissolve the Cu precipitates, and then transform back to martensite upon cooling to room temperature. After a solution annealing treatment, Cu that was dissolved into the martensite matrix during the solution anneal is precipitated via aging heat treatments up to 620°C that produce varying precipitate morphologies associated with various strength levels[44].

Noting the stability of these various phases, only the nano-scale Cu precipitate is expected to be evolving between the H900 and H1025 heat treatments (Table 2). Given that fatigue behavior is relatively insensitive to strength level in steels[92] and that Cu precipitation should be relatively homogenous[67], the Cu precipitates are an unlikely cause for the observed fatigue crack growth behavior in the 17-4PH rod. Still, there was a clear effect of heat treatment, so treatments that would modify other phases were tested. Namely, the AR condition was tested to represent a Cu precipitate free alloy, and a SA treatment was tested to re-

crystallize the martensite structure. The results from these treatments were consolidated with previous experiments to show the effect of heat treatment on the 17-4PH rod fatigue crack growth phenomena (Fig. 9).

Interestingly, the AR and SA conditions, both solution annealed with Cu precipitates dissolved, exhibited vastly different fatigue crack growth behaviors. In the AR condition, the most severe case of crack growth rate reduction was encountered with crack arrest occurring at a/W = 0.39. Conversely, the SA condition exhibited a nominally constant crack growth rate across the entire range of tested a/W. These results indicate that Cu precipitate evolution cannot be linked to the decelerating growth rate at a/W = 0.39 since they were not present. However, these results do reveal a different trend; the reduction in growth rate is attenuated by increasing exposure to elevated temperatures. One characteristic that is known to reduce/relax with high temperature exposure is residual stress[93]. Residual stress may also influence the fatigue crack growth rate through modification of the local stress state at the crack tip and is, therefore, a potential cause for the fatigue behavior in the 17-4PH rod.

3.4 Residual Stress in the 17-4PH Rod

To test the hypothesis that residual stress (RS) might be the root cause of the anomalous 17-4PH rod growth rate behavior, the various samples used to produce the growth rates in Fig. 9 were evaluated for RS via the slitting method (Fig. 10). With a peak tensile/compressive RS of +410/-160 MPa, the AR condition rod has the most significant levels of RS. Consistent with the results in Fig. 9, the RS subsides

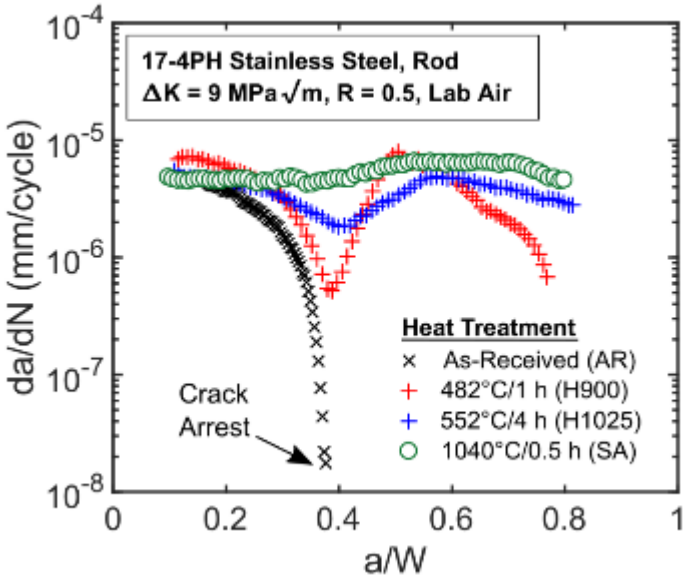

Fig. 9 | **Effect of heat treatment on fatigue crack growth in 17-4PH rod.** Fatigue crack growth rates are compared for 17-4PH rod in the as-received (AR) condition and heat treated to the H900, H1025, and SA conditions. Growth rates were captured as a function of a/W at a constant ΔK = 9 MPa√m, R = 0.5.

with increasing exposure to heat with peak tensile/compressive RS minimized at +130/-90 MPa in the SA condition. The corresponding residual stress intensities (K_{RS}) may then be plotted as a function of *a/W* (Fig. 10b). Comparison of the K_{RS} results with the growth rate results in Fig. 9 show correlations between compressive RS and growth rate reductions; this correlation suggests that residual stress is playing a salient role in modifying the crack growth rate via mechanical superposition. Further, the peak compressive K_{RS}

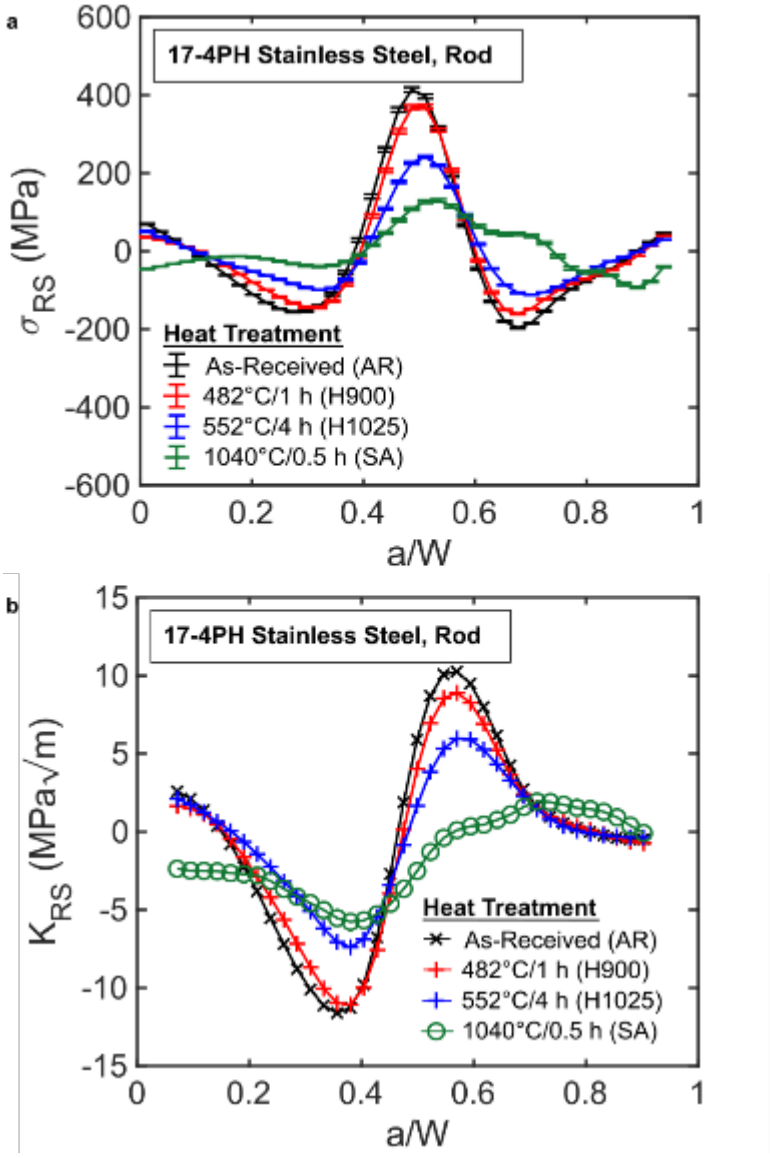

Fig. 10 | **Residual stress and stress intensity in various conditions of 17-4PH rod**. **a**, Residual stresses (σ_{RS}). **b**, Residual stress intensity factors (K_{RS}). Residual stresses and stress intensity factors are shown as a function of *a/W* for 17-4PH rod in various heat treatment conditions. All residual stresses shown were gathered via the slitting method.

coincides at approximately the same *a/W* as the minimum growth rate zone for each heat treatment; even the slight shift of that minimum to higher *a/W* with elevated temperature heat treatment is reflected in the RS distribution. However, these correlations break down in two ways. First, there is a near-negligible difference between the AR and H900 RS magnitudes, yet there is over an order of magnitude difference in growth rate at *a/W* ~ 0.39 in Fig. 9. Second, at *a/W* > 0.5 the K_{RS} is primarily tensile (Fig. 10b) and should increase growth rates, but the measured growth rates drop (Fig. 9). These two observations suggest that mechanism(s) beyond a simple superposition of RS mechanical driving forces are modifying the crack growth rates.

As previously mentioned, closure can decelerate fatigue crack propagation by reducing the mechanical driving force via crack wake impingement. Topographic mapping (Fig. 11) of the various crack wakes in Fig. 9 demonstrates that the non-flat crack path highlighted in Fig. 4 is modified by heat treatment. Specifically, the magnitude of the twist in the crack path was reduced with increased heat treatment time/temperature (Fig. 11a) and the corresponding reduction in residual stress magnitude (Fig. 10a). This twist was then quantified by fitting a line profile across the fracture surface thickness at various *a/W* and calculating the angle of the crack path with respect to the Mode I fracture plane (Fig. 11b). Additionally, those same line profiles were used to quantify the roughness (*Rq*) of the crack path as a function of *a/W*. Reviewing the trends across these datasets shows a general reduction in both twist and surface roughness of the fracture surface with increasing heat treatment time/temperature. These downward trends are consistent with the crack growth rates in Fig. 9 and suggest that the crack wake closure could have been occurring both microscopically and macroscopically via crack wake roughness and impingement, respectively. More precisely, the increase in roughness could have led to closure at the crack tip, and the wake twist could have led to closure through impingement behind the crack tip. Additionally, the twist of the crack path could have led to a direct reduction of the crack tip mechanical driving force through deflection as mentioned in Section 3.2.

To further quantify the effect of residual stress on the 17-4PH fatigue crack growth rate, the NASGRO equation was utilized to simulate the previously (empirically) evaluated effects of heat treatment and stress ratio, see Fig. 12. As might be expected given the K_{RS} values, there is good correlation in the simulated crack growth rate trends with the K_{RS} trends in Fig. 10b below *a/W* = 0.5. This indicates that the initial crack growth rate phenomenon is substantially driven by the residual stresses within the 17-4PH rod. However, the accuracy of the simulation again breaks down in two ways: (i) the crack growth rate drop magnitudes are underpredicted by the simulation and (ii) the crack growth rate reductions beyond *a/W* = 0.5 are not captured. These gross differences further support the presence of additional growth rate modifying mechanisms. The simulation assumed a flat, Mode I crack path, so the postulated crack

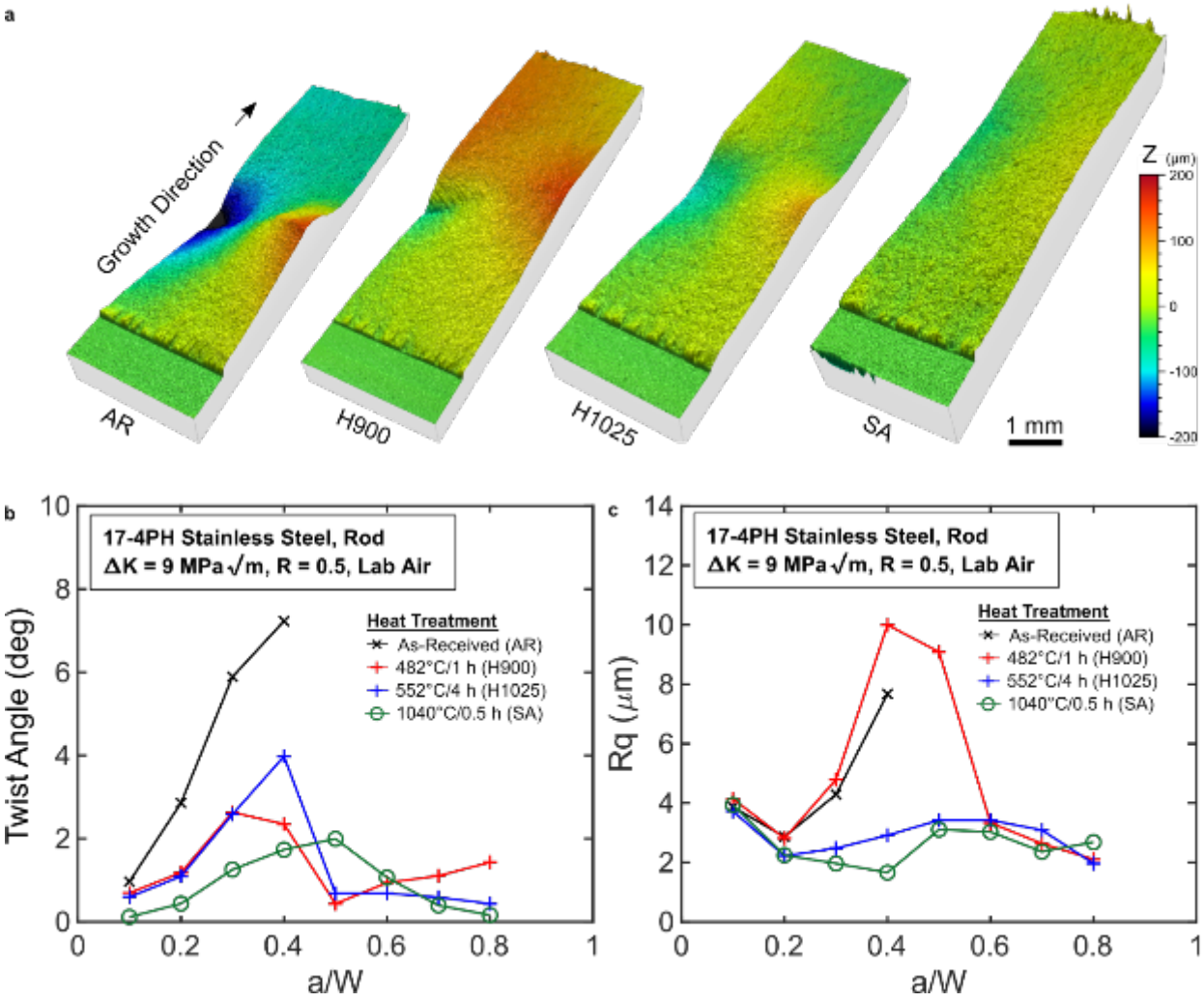

Fig. 11 | **Variation in fracture surface topography induced by heat treatment of 17-4PH rod**. **a**, Fracture surface topographic height (*Z*) maps. **b**, Fracture surface twist angle variations. **c**, Fracture surface roughness (*Rq*) variations. Fatigue fracture surfaces for various conditions of 17-4PH rod (i.e., AR, H900, H1025, SA) were topographically mapped as a function of *a/W* (**a**). Line profiles traversing across the fracture surface thickness (i.e., *B*) at various *a/W* were used to calculate twist angle (**b**) and roughness variations (**c**). All fatigue cracks shown were grown at a constant ΔK = 9 MPa$\sqrt{m}$, R = 0.5 in lab air. Note that the 1 mm scalebar in (**a**) only applies to planar dimensions; Z height is exaggerated for clarity.

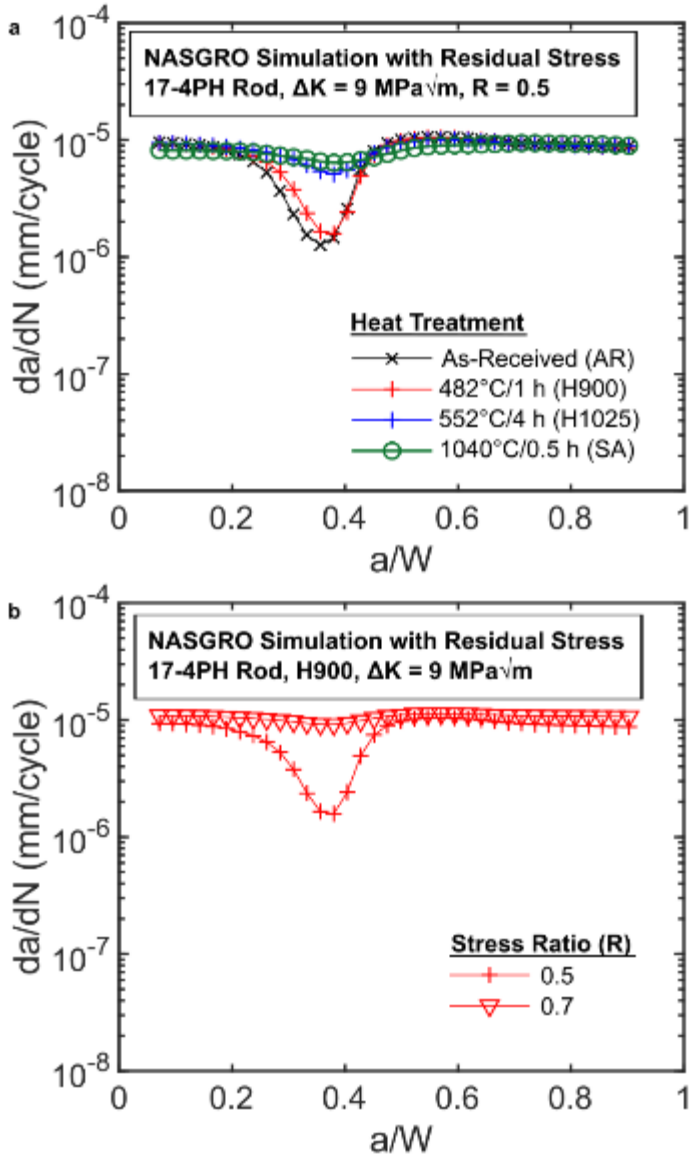

Fig. 12 | **Simulated effects of measured residual stresses on fatigue crack growth in 17-4PH rod**. **a**, Simulated heat treatment effect. **b**, Simulated stress ratio effect. Fatigue crack growth rates are simulated using the NASGRO equation with the inclusion of measured residual stress profiles. The simulations attempt to replicate experimental fatigue growth gathered for the 17-4PH rod under various heat treatments (**a**) and applied stress ratios (**b**) at a nominal, constant ΔK = 9 MPa√m.

wake-based closure and deflection-based mechanical driving force modifications remain likely culprits for these simulation breakdowns. Additionally, this simulation did not consider elastic deflections in the crack wake that may be induced via the residual stresses in the bulk (i.e., a separate effect from the simulated K_{RS} superposition at the crack tip). It has been demonstrated that these residual stress-induced deflections can cause impingement in the crack wake thus modifying the total stress intensity via a contact pressure effect[77,94].

The presence of residual stress and its effect on the fatigue crack growth behavior of 17-4PH rod has been demonstrated, but the origin of the residual stress has not yet been clarified. The first possible origin for the RS is the centerless grinding step used to finish the surface of the rod. It is well known that grinding can produce residual stresses, but these are typically limited to the first 100 μm below a ground surface[95]. Rather, the shape of the AR residual stress profile (Fig. 10a) follows the classical shape of quench-induced RS where non-uniform cooling after heat treatment produces tensile, axial RS near the centerline of a cross-section (a/W = 0.5 in this case) balanced by compressive stresses near the edges[24,25]. Therefore, residual stresses might have formed during the air-cool quench that followed the last heat treatment performed on the AR material. However, previous work has shown that air-cooling from ~1000°C produces negligible residual stresses in 20 mm diameter round rods of both 1010 carbon steel[96] and IN718[26] which suggests a different source for the RS in the current 15.9 mm diameter 17-4PH. This contradiction is clarified by comparing the AR and SA processing steps and RS profiles in Fig. 10a. These conditions both represent solution annealing heat treatments (i.e., 1040°C, air-cool quench), yet the RS profiles are drastically different. The SA residual stress profile is of a negligible magnitude as would be expected from an air cool, but the AR condition has significant RS. The primary difference between the AR and SA material is that the SA material was locally heat treated by the authors whereas the AR material was heat treated by the manufacturer. Given the classical quench-induced RS profile shape for the AR material, it is most likely that the manufacturers erroneously quenched the rod in a fast-cooling medium (e.g., water or oil), rather than the reported air-cooling method, thereby inducing residual stress in the 17-4PH rod.

To summarize, residual stress has been identified in 17-4PH rod and linked to various, anomalous fatigue behaviors in the material. Classical quenching-induced residual stresses have been shown to induce out-of-plane cracking and roughened crack paths that significantly modify fatigue crack growth rates. Further, the mechanical superposition-based mechanism commonly used to account for residual stress effects was complicated by second-order crack path-based modifiers to the growth rate. Specifically, the crack path likely induced (1) crack wake roughness-induced closure, (2) crack wake impingement-induced closure, and (3) crack deflection-based modification of the mechanical driving force. Critically, the root cause of these behaviors is the non-Mode I crack path induced by residual stress, but the details describing how the residual stress resulted in this irregular crack front remain unclear. Detailed, predictive analyses of the crack path evolution were not performed in the current work, but it is likely that 3D residual stress states led to the observed crack paths. The current study evaluated the magnitude and distribution of axial residual stresses, but Dye et al.[26] have demonstrated that quenching-induced residual stresses in a round rod also have significant radial and circumferential stress components. With this, the current study indicates that the 3D residual stress state induced by quenching of rod round may produce 3D crack paths which strongly modify the fatigue crack growth rate.

3.5 Implications of this Work

There are several practical implications that result from this work. First, material product form is a low-resolution descriptor for fatigue behavior differences that can occur between two forms of a single alloy. The current work has shown that significant differences in the fatigue crack growth rate of 17-4PH plate and rod were better described via quantification of residual stress. Second, residual stress has been shown to produce significant fatigue behavior differences via crack path modification. In particular, 3D quench-induced residual stresses can produce a 3D fatigue crack path twist that significantly affects the fatigue crack growth rate via a combination of closure and crack-deflection effects. Critically, these crack path fluctuations can occur on the meso-scale (i.e., ~400 μm peak-to-peak) rather than the more commonly studied micro-scale[40,97] or macro-scale[14,33,98]. Currently, most engineering analyses of fatigue cracks assume a flat crack path, so this interaction of 3D residual stresses, non-planar crack paths, and closure poses a challenge for the modeling community. Third, these effects are persistent even when subjected to several modification strategies. Various extrinsic factors that are known to have impacts on fatigue crack growth behavior were systematically evaluated including the effect of: stress intensity gradients, crack tip constraint, stress ratio, test environment, and material heat treatment. The severity of the residual stress impacts decreased for high R conditions and after heat treatment at high temperatures, but the effect of residual stress persisted through stress intensity gradient modifications, crack tip constraint modifications, stress ratio modifications, and test environment modifications. These various observations highlight (1) residual stress is a powerful coupon-scale feature, and (2) that residual stress can dominate the fatigue crack growth behavior of a material even when confronted with various extrinsic modification strategies. It is important to recognize the persistent nature of the residual stress for both engineering applications and laboratory testing. The presence of residual stress must be considered and/or accounted for in order to ensure that the engineering structural integrity analysis and laboratory data fidelity are not compromised.

4.0 Conclusions

Fracture mechanics-based fatigue crack growth rate testing was used to compare the fatigue behavior of two forms of 17-4PH stainless steel. Characterization of the “rod” and “plate” product forms revealed several anomalous fatigue behaviors in the rod at constant applied ΔK including a variable crack growth rate and a twisted, 3D crack path. To interrogate this behavior, a number of extrinsic modifiers were applied to the fatigue process and characterized with the following conclusions:

- Residual stress present in 17-4PH rod was correlated with fatigue crack growth rate modifications, crack path deflections from a nominal Mode I crack path, and roughness/topography induced fatigue crack closure.

- Residual stresses in the 17-4PH rod were maximum in the "as-received" conditions (i.e., from the manufacturer) and attenuated with increasing heat treatment time and temperature. After a solution annealing treatment (1040°C/0.5 h), the residual stress field was largely removed, but remnants of residual stress were still apparent.
- Impacts on the fatigue crack growth rate from the residual stress field could be simulated via the NASGRO equation, but errors in the simulation were attributed to crack deflection effects and roughness/topography induced closure at long crack lengths (i.e., high *a/W*).
- Increased crack tip constraint via fracture specimen side-grooving and bulk T-stress modifications (i.e., modified SENT loading configurations) were insufficient to alleviate fatigue crack path deflection attributed to residual stresses.
- High heat treatment time/temperature (1040°C/0.5 h) was the most effective way to alleviate the residual stress induced fatigue behavior modifications in 17-4PH rod.

5.0 Acknowledgements

This research was financially supported by the Office of Naval Research under Grant No. N00014-18-1-2427 with Dr. Airan Perez as the Scientific Officer and by NASA Space Technology Research Fellowship Grant Number 80NSSC19K1132.

6.0 References

1. Stephens, R. ., Fatemi, A., Stephens, R. R. & Fuchs, H. O. *Metal Fatigue in Engineering*. (John Wiley & Sons, 2001).
2. Maddox, S. J. Fatigue design rules for welded structures. *Prog. Struct. Eng. Mater.* **2**, 102–109 (2000).
3. Macdonald, K. A. & Maddox, S. J. New guidance for fatigue design of pipeline girth welds. *Eng. Fail. Anal.* **10**, 177–197 (2003).
4. Tavares, S. M. O. & de Castro, P. M. S. T. An overview of fatigue in aircraft structures. *Fatigue Fract. Eng. Mater. Struct.* **40**, 1510–1529 (2017).
5. Jones, R. Fatigue crack growth and damage tolerance. *Fatigue Fract. Eng. Mater. Struct.* **37**, 463–483 (2014).
6. ASTM International. ASTM E647-15e1 Standard Test Method for Measurement of Fatigue Crack Growth Rates. (2015). doi:10.1520/E0647-15E01
7. Anderson, T. L. *Fracture Mechanics: Fundamentals and Applications*. (CRC Press, 2005).

doi:10.1201/9781420058215

8. Gallagher, J. *MCIC-HB-01R Damage Tolerant Design Handbook. A Compilation of Fracture and Crack-Growth Data for High-Strength Alloys*. (1983).

9. Sadananda, K., Nani Babu, M. & Vasudevan, A. K. A review of fatigue crack growth resistance in the short crack growth regime. *Mater. Sci. Eng. A* **754**, 674–701 (2019).

10. Jones, R., Singh Raman, R. K. & McMillan, A. J. Crack growth: Does microstructure play a role? *Eng. Fract. Mech.* **187**, 190–210 (2018).

11. Skorupa, M. Load Interaction Effects During Fatigue Crack Growth Under Variable Amplitude Loading — a Literature Review . Part I : Empirical Trends. *Fatigue Fract. Eng. Mater. Struct.* **21**, 987–1006 (1998).

12. Ronevich, J. A., Elia, C. R. D. & Hill, M. R. Fatigue crack growth rates of X100 steel welds in high pressure gas considering residual stress effects. *Eng. Fract. Mech.* **194**, 42–51 (2018).

13. Ronevich, J. A. *et al.* Fatigue crack growth rates in high pressure hydrogen gas for multiple X100 pipeline welds accounting for crack location and residual stress. *Eng. Fract. Mech.* **228**, 106846 (2020).

14. Pook, L. P. A 50-year retrospective review of three-dimensional effects at cracks and sharp notches. *Fatigue Fract. Eng. Mater. Struct.* **36**, 699–723 (2013).

15. Vasudevan, A. K. & Sadananda, K. Classification of environmentally assisted fatigue crack growth behavior. *Int. J. Fatigue* **31**, 1696–1708 (2009).

16. Pippan, R. & Hohenwarter, A. Fatigue crack closure: a review of the physical phenomena. *Fatigue Fract. Eng. Mater. Struct.* **40**, 471–495 (2017).

17. James, L. A. Fatigue crack propagation in alloy 718: a review. in *Superalloy 718-Metallurgy and Applications* (ed. Loria, E. A.) 599–515 (MM&MS, 1989).

18. James, L. A. *The Effect of Temperature on the Fatigue-Crack Propagation Behavior of A-286 Steel*. (1976). doi:https://doi.org/10.2172/4059538

19. Gall, K. *et al.* Effect of microstructure on the fatigue of hot-rolled and cold-drawn NiTi shape memory alloys. *Mater. Sci. Eng. A* **486**, 389–403 (2008).

20. Kaufman, J. G. *Properties of Aluminum Alloys: Fatigue Data and Effects of Temperature, Product Form, and Processing*. (ASM International, 2008).

21. Venkateswara Rao, K. T., Bucci, R. J., Jata, K. V. & Ritchie, R. O. A comparison of fatigue-crack

propagation behavior in sheet and plate aluminum-lithium alloys. *Mater. Sci. Eng. A* **141**, 39–48 (1991).

22. Saxena, V. K. & Radhakrishnan, V. M. Effect of Wrought Product Thickness and Stress Ratio on Fatigue Crack Growth Behavior of a Quaternary Aluminium-Lithium Alloy. *J. Eng. Mater. Technol.* **121**, 393–398 (1999).

23. Bush, R. W., Bucci, R. J., Magnusen, P. E. & Kuhlman, G. W. Fatigue crack growth rate measurements in aluminum alloy forgings: Effects of residual stress and grain flow. *ASTM Spec. Tech. Publ.* 568–589 (1993). doi:10.1520/stp24289s

24. Alpsten, G. A. *Thermal residual stresses in hot-rolled steel members*. (1968).

25. Robinson, J. S., Tanner, D. A. & Truman, C. E. 50th anniversary article: The origin and management of residual stress in heat-treatable aluminium alloys. *Strain* **50**, 185–207 (2014).

26. Dye, D., Conlon, K. T. & Reed, R. C. Characterization and modeling of quenching-induced residual stresses in the nickel-based superalloy IN718. *Metall. Mater. Trans. A Phys. Metall. Mater. Sci.* **35 A**, 1703–1713 (2004).

27. Abambres, M. & Quach, W. M. Residual stresses in steel members: A review of available analytical expressions. *Int. J. Struct. Integr.* **7**, 70–94 (2016).

28. Smudde, C. M., Elia, C. R. D., San, C. W., Hill, M. R. & Gibeling, J. C. The influence of residual stress on fatigue crack growth rates of additively manufactured Type 304L stainless steel. *Int. J. Fatigue* **162**, 106954 (2022).

29. Edwards, L. Influence of residual stress redistribution on fatigue crack growth and damage tolerant design. *Mater. Sci. Forum* **524**–**525**, 363–372 (2006).

30. Zhang, H. *et al.* Fatigue crack growth in residual stress fields of laser shock peened Ti6Al4V titanium alloy. *J. Alloys Compd.* **887**, 161427 (2021).

31. Beghini, M., Bertini, L. & Vitale, E. Fatigue Crack Growth in Residual Stress Fields: Experimental Results and Modeling. *Fatigue Fract. Eng. Mater. Struct.* **17**, 1433–1444 (1994).

32. Schnubel, D. & Huber, N. The influence of crack face contact on the prediction of fatigue crack propagation in residual stress fields. *Eng. Fract. Mech.* **84**, 15–24 (2012).

33. Ma, Y. E., Liu, B. Q. & Zhao, Z. Q. Crack paths in a friction stir-welded pad-up for fuselage applications. *J. Aircr.* **50**, 879–885 (2013).

34. Predan, J., Pippan, R. & Gubeljak, N. Fatigue crack propagation in threshold regime under residual

stresses. *Int. J. Fatigue* **32**, 1050–1056 (2010).

35. Gallagher, J. P., Giessler, F. J., Berens, A. P. & Engle, R. M. *AFWAL-TR-82-3073 USAF Damage Tolerant Design Handbook: Guidelines for the Analysis and Design of Damage Tolerant Aircraft Structures*. (1984).

36. Spagnoli, A., Carpinteri, A. & Vantadori, S. On a kinked crack model to describe the influence of material microstructure on fatigue crack growth. *Frat. ed Integrita Strutt.* **25**, 94–101 (2013).

37. Spradlin, T. J. & Hodges, J. L. Predictive Crack Growth Technique for Laser Peening Process Development. *J. Eng.* **2015**, 138–143 (2015).

38. Xue, L. & Wierzbicki, T. Numerical simulation of fracture mode transition in ductile plates. *Int. J. Solids Struct.* **46**, 1423–1435 (2009).

39. Geng, M., Chen, H., Yang, Y. & Li, Y. Prediction of crack shape in a cylindrical bar under combined fatigue tension and torsion loading. *Theor. Appl. Fract. Mech.* **109**, 102727 (2020).

40. Suresh, S. Fatigue crack deflection and fracture surface contact: Micromechanical models. *Metall. Trans. A* **16**, 249–260 (1985).

41. Forth, S. C., Herman, D. J., James, M. A. & Johnston, W. M. Fatigue crack growth rate and stress-intensity factor corrections for out-of-plane crack growth. *J. ASTM Int.* **2**, 1–14 (2005).

42. Zerbst, U. *et al.* Safe life and damage tolerance aspects of railway axles - A review. *Eng. Fract. Mech.* **98**, 214–271 (2013).

43. Kadhim, M. H., Latif, N. A., Harimon, M. A., Shamran, A. A. & Abbas, D. R. Effects of side-groove and loading rate on the fracture properties of aluminium alloy AL-6061. *Materwiss. Werksttech.* **51**, 758–765 (2020).

44. ASTM International. ASTM A693-16 Standard Specification for Precipitation-Hardening Stainless and Heat-Resisting Steel Plate, Sheet, and Strip. (2016).

45. ASTM International. ASTM E8/E8M-16a Standard Test Methods for Tension Testing of Metallic Materials. (2016). doi:https://doi.org/10.1520/E0008_E0008M-16A

46. ASTM International. ASTM E384-17 Standard Test Method for Microindentation Hardness of Materials. (2017).

47. ASTM International. ASTM E140-12b Standard Hardness Conversion Tables for Metals Relationship Among Brinell Hardness, Vickers Hardness, Rockwell Hardness, Superficial Hardness, Knoop Hardness, Scleroscope Hardness, and Leeb Hardness. (2019).

48. Bachmann, F., Hielscher, R. & Schaeben, H. Texture Analysis with MTEX - Free and Open Source Software Toolbox. *Solid State Phenom.* **160**, 63–68 (2010).

49. Nyyssönen, T., Peura, P. & Kuokkala, V. T. Crystallography, Morphology, and Martensite Transformation of Prior Austenite in Intercritically Annealed High-Aluminum Steel. *Metall. Mater. Trans. A Phys. Metall. Mater. Sci.* **49**, 6426–6441 (2018).

50. Donald, J. K. & Ruschau, J. Direct Current Potential Difference Fatigue Crack Measurement Techniques. *Fatigue Crack Meas. Tech. Appl.* 11–38 (1991).

51. ASTM International. ASTM E399-19 Standard Test Method for Linear-Elastic Plane-Strain Fracture Toughness K1c of Metallic Materials. (2019).

52. Tada, H., Paris, P. C. & Irwin, G. R. *The Stress Analysis of Cracks Handbook, Third Edition*. (ASME, 2000). doi:10.1115/1.801535

53. Freed, C. N. & Krafft, J. M. Effect of Side Grooving on Measurements of Plane-Strain Fracture Toughness. *J. Mater.* **1**, 770–790 (1966).

54. Zhu, X. K. Full-range stress intensity factor solutions for clamped SENT specimens. *Int. J. Press. Vessel. Pip.* **149**, 1–13 (2017).

55. Johnson, H. H. Calibrating the Electric Potential Method for Studying Slow Crack Growth. *Mater. Res. Stand.* **5**, 442–445 (1965).

56. ASME. ASME B46.1-2009: Surface Texture (Surface Roughness, Waviness, and Lay). (2009).

57. Hill, M. R. The Slitting Method. in *Practical Residual Stress Measurement Methods* (ed. Schajer, G. S.) (John Wiley & Sons, 2013).

58. Prime, M. B. Residual stress measurement by successive extension of a slot: the crack compliance method. *Appl. Mech. Rev.* **52**, 75–96 (1999).

59. Schindler, H., Cheng, W. & Finnie, I. Experimental Determination of Stress Intensity Factors Due to Residual Stresses. *Exp. Mech.* **37**, 272–277 (1997).

60. Schajer, G. S. & Prime, M. B. Use of Inverse Solutions for Residual Stress Measurements. *J. Eng. Mater. Technol.* **128**, 375–382 (2006).

61. Schindler, H. J. & Bertschinger, P. Some steps towards automation of the crack compliance method to measure residual stress distributions. *Proc. 5th Int. Conf. Res. Stress. ICRS-5* **1**, 682–687 (1997).

62. Olson, M. D. & Hill, M. R. Two-Dimensional Mapping of In-plane Residual Stress with Slitting. *Exp. Mech.* **58**, 151–166 (2018).

63. Prime, M. B. & Hill, M. R. Uncertainty, model error, and order selection for series-expanded, residual-stress inverse solutions. *J. Eng. Mater. Technol.* **128**, 175–185 (2006).

64. Forman, R. G. & Mettua, S. R. *(NASA-TM-102165) Behavior of Surface and Corner Cracks Subjected to Tensile and Bending Loads in Ti-6Al-4V Alloy*. (1990).

65. Beek, J. M. *NASGRO Reference Manual, Version 9.1*. (NASA Johnson Space Center, 2019).

66. Newman, J. C. A crack opening stress equation for fatigue crack growth. *Int. J. Fract.* **24**, 131–135 (1984).

67. Viswanathan, U. K., Banerjee, S. & Krishnan, R. Effects of aging on the microstructure of 17-4 PH stainless steel. *Mater. Sci. Eng. A* **104**, 181–189 (1988).

68. ASTM International. ASTM A564/A564M-19a Standard Specification for Hot-Rolled and Cold-Finished Age-Hardening Stainless Steel Bars and Shapes. (2019).

69. Hockauf, K., Hockauf, M., Wagner, M. F. X., Lampke, T. & Halle, T. Fatigue crack propagation in an ECAP-processed aluminium alloy - Influence of shear plane orientation. *Materwiss. Werksttech.* **43**, 609–616 (2012).

70. Srinath, J. *et al.* Metallurgical Analysis of a Failed 17-4 PH Stainless Steel Pyro Bolt Used in Launch Vehicle Separation Systems. *Mater. Perform. Charact.* **4**, MPC20140063 (2015).

71. Zuidema, J., Veer, F. & Van Kranenburg, C. Shear lips on fatigue fracture surfaces of aluminum alloys. *Fatigue Fract. Eng. Mater. Struct.* **28**, 159–167 (2005).

72. Shlyannikov, V. N. T -stress for crack paths in test specimens subject to mixed mode loading. *Eng. Fract. Mech.* **108**, 3–18 (2013).

73. Wang, J. *et al.* Effect of δ -ferrite on the stress corrosion cracking behavior of 321 stainless steel. *Corros. Sci.* **158**, 108079 (2019).

74. Burns, J. T. *et al.* Effect of water vapor pressure on fatigue crack growth in Al-Zn-Cu-Mg over wide-range stress intensity factor loading. *Eng. Fract. Mech.* **137**, 34–55 (2015).

75. Meggiolaro, M. A. Stress intensity factor equations for branched crack growth. *Eng. Fract. Mech.* **72**, 2647–2671 (2005).

76. Ritchie, R. O. Mechanism of Fatigue-Crack Propagation in Ductile and Brittle Materials. *Int. J. Fract.* **100**, 55–83 (1998).

77. Hill, M. R. & Kim, J. Fatigue Crack Closure in Residual Stress Bearing Materials. *J. ASTM Int.* **9**, (2011).

78. Williams, M. L. On the Stress Distribution at the Base of a Stationary Crack. *J. Appl. Mech.* **24**, 109–114 (1957).

79. Gupta, M., Alderliesten, R. C. & Benedictus, R. A review of T-stress and its effects in fracture mechanics. *Eng. Fract. Mech.* **134**, 218–241 (2015).

80. Leevers, P. S. & Radon, J. C. Inherent stress biaxiality in various fracture specimen geometries. *Int. J. Fract.* **19**, 311–325 (1982).

81. Suresh, S. *Fatigue of Materials*. (Cambridge University Press, 1998).

82. Johnson, F. A. & Radon, J. C. Mechanical and Metallurgical Aspects of Fracture Behavior of an Al-Alloy. *Int. J. Fract. Mech.* **8**, 21–36 (1972).

83. Zhu, X. K. & Joyce, J. A. Review of fracture toughness (G, K, J, CTOD, CTOA) testing and standardization. *Eng. Fract. Mech.* **85**, 1–46 (2012).

84. Liu, Z., Yu, D., Tang, J., Chen, X. & Wang, X. Stress intensity factor and T-stress solutions for three-dimensional clamped single edge notched tension (SENT) specimens. *Int. J. Press. Vessel. Pip.* **168**, 11–23 (2018).

85. Saxena, A., Bassi, F., Nibur, K. & Newman, J. C. On single-edge-crack tension specimens for tension-compression fatigue crack growth testing. *Eng. Fract. Mech.* **176**, 343–350 (2017).

86. Petit, J., Hénaff, G. & Sarrazin-Baudoux, C. Environmentally Assisted Fatigue in the Gaseous Atmosphere. in *Comprehensive Structural Integrity* **6**, 211–280 (Elsevier, 2003).

87. Antony, K. C. Aging Reactions in Precipitation Hardenable Stainless Steel. *J. Met.* 922–927 (1963).

88. Herrera Lara, V., Guerra Fuentes, L., Covarrubias Alvarado, O., Salinas Rodriguez, A. & Garcia Sanchez, E. Hot Ductility of the 17-4 PH Stainless Steels. *J. Mater. Eng. Perform.* **25**, 1041–1046 (2016).

89. Lass, E. A., Zhang, F. A. N. & Campbell, C. E. Nitrogen Effects in Additively Manufactured Martensitic Stainless Steels : Conventional Thermal Processing and Comparison with Wrought. *Metall. Mater. Trans. A* **51**, 2318–2332 (2020).

90. Ludwigson, D. C. & Hall, A. M. *DMIC Report 111 The Physical Metallurgy of Precipitation-Hardenable Stainless Steels*. (1959).

91. Pollard, B. Selection of Wrought Precipitation-Hardening Stainless Steels. *ASM Handb. Welding, Brazing, Solder.* **6**, 482–494 (1993).

92. Barsom, J. M. Fatigue-Crack Propagation in Steels of Various Yield Strengths. *J. Eng. Ind.* **93**,

1190–1196 (1971).

93. Wang, Z., Chen, Y. & Jiang, C. Thermal relaxation behavior of residual stress in laser hardened 17-4PH steel after shot peening treatment. *Appl. Surf. Sci.* **257**, 9830–9835 (2011).

94. Jones, K. W. & Dunn, M. L. Fatigue crack growth through a residual stress field introduced by plastic beam bending. *Fatigue Fract. Eng. Mater. Struct.* **31**, 863–875 (2008).

95. Koster, W. P., Field, M., Fritz, L. J., Gatto, L. R. & Kahles, J. F. *AFML-TR-70-11 Surface Integrity of Machined Structural Components*. (1970).

96. Boyadjiev, I. I., Thomson, P. F. & Lam, Y. C. Prediction of the deflection and residual stress in controlled cooling of hot-rolled steel beams including load and arbitrary support Part II . Experimental validation and application. *J. Mater. Process. Technol.* **147**, 268–275 (2004).

97. Igwemezie, V., Dirisu, P. & Mehmanparast, A. Critical assessment of the fatigue crack growth rate sensitivity to material microstructure in ferrite-pearlite steels in air and marine environment. *Mater. Sci. Eng. A* **754**, 750–765 (2019).

98. Miranda, A. C. O., Meggiolaro, M. A., Castro, J. T. P., Martha, L. F. & Bittencourt, T. N. Fatigue life and crack path predictions in generic 2D structural components. *Eng. Fract. Mech.* **70**, 1259–1279 (2003).